Allosteric regulation of TRPV1 by the inflammatory lipid LPA

William R. Arnold[1], David Julius[2]*, and Yifan Cheng[1,3]*

1. Department of Biochemistry and Biophysics, University of California San Francisco, 600 16th St. San Francisco, CA, 94158
2. Department of Physiology, University of California San Francisco, 600 16th St. San Francisco, CA, 94158
3. Howard Hughes Medical Institute, University of California San Francisco, San Francisco, CA 94158

*corresponding authors

Keywords: cryo-EM, lysophosphatidic acid, transient receptor potential vanilloid 1, allostery

ABSTRACT

Transient Receptor Potential Vanilloid 1 (TRPV1) is a tetrameric cation channel expressed in primary afferent neurons, where it contributes to thermosensation and nociception. TRPV1 is a polymodal signal integrator that responds not only to heat, but also to inflammatory agents that produce pain hypersensitivity, including bioactive lipids such as endocannabinoids or lysophosphatidic acid (LPA). Cryo-EM structures have revealed how exogenous ligands, such as capsaicin or drugs, vanilloid bind to and activate TRPV1, but a detailed molecular understanding regarding the actions of endogenous inflammatory lipids remain scarce. Here, we describe how LPA binds to and activates TRPV1 by visualizing multiple ligand-channel substates. These structural data demonstrate that LPA binds cooperatively to TRPV1 and allosterically induces conformational changes that drive channel opening. We These data provide valuable insight into the function of inflammatory lipids on TRPV1 and provides further mechanistic insight into how endogenous agonists activate this channel.

INTRODUCTION

TRPV1 is a polymodal excitatory cation channel expressed by somatosensory neurons that is activated by heat and inflammatory agents, including extracellular protons and numerous inflammatory lipids such as lysophosphatidic acid (LPA)[1-5]. Indeed, the role of TRPV1 in mediating inflammatory pain reflects its ability to be activated or modulated by this distinct physiologic stimuli[6-8]. LPA is an important bioactive lipid that mediates a host of biological responses, including cellular migration and proliferation, inflammation, and pain[9]. While LPA is known to activate metabotropic receptors (GPCRs), it has also been shown to activate or potentiate ionotropic receptors, including TRPV1[9-11]. Indeed, LPA has been shown to elicit TRPV1-evoked pain in mice[11] and to directly activate recombinant TRPV1 channels in reconstituted liposomes[12].

While a functional connection between LPA and TRPV1 is well established, little is known about how this ligand bind to TRPV1 and elicits channel gating. Mutagenesis studies have implicated a residue (lysine 710, K710) near the C-terminal 'TRP box' domain of the channel as being critical for LPA sensitivity[11], but whether this residue is directly involved in ligand binding has not been ascertained.

So far, all other lipophilic agonists have been observed to bind within a key regulatory pocket that serves as the binding site for capsaicin and other vanilloid ligands. This vanilloid binding pocket (VBP) is located within an 'elbow' between the voltage sensor-like domain (S1-S4) and the central pore-forming unit (S5-S6)[13-19]. Structural data show that binding of agonist to this site, competitively displacing an endogenous resident phosphoinositide (PI) lipid, is a key step in channel activation[14,16-18]. Because K710 is approximately 20 Å away from the VBP, where most other known agonists bind, it is not clear how mutation of this residue affects LPA action.

To address this question, we use single-particle cryo-EM to determine the site of LPA binding and how it promotes an open channel state. Specifically, we describe 6 conformational states representing different ligand binding stoichiometries. We show that LPA binds to the VBP, whereby it competes for

binding with the resident PI lipid, similar to what we have observed with vanilloid ligands. These structures also provide evidence for cooperative binding of LPA and allosteric effects on channel gating. Together, these data provide valuable insight into how an endogenous inflammatory lipid regulates a critical nociceptive ion channel.

RESULTS and DISCUSSION

Structures of LPA bound to TRPV1

We reconstituted a minimal functional TRPV1 channel[12] into lipid nanodiscs, added LPA in a molar ratio of 25:3 (LPA:TRPV1), and determined a consensus cryo-EM map with C4 symmetry to a resolution of 3.0 Å. In this initial consensus map, we did not observe LPA-like density near K710 but instead observed density within the VBP that was distinct from that of the endogenous (resident) PI lipid. . Classification of C4 symmetrized particles did not separate those with bound LPA versus PI lipid and thus indicated that LPA binding to the channel may be heterogenous and sub-stoichiometric.

To classify particles with sub-stoichiometric LPA binding, we first symmetry expanded tetrameric TRPV1 particles and then applied focused classification on the VBP for each individual monomer of the channel, yielding two major conformations of monomeric TRPV1 reconstructions with either endogenous PI or applied LPA bound in the VPB (Supplementary Figure 1). The major hallmarks that differentiate the VBP containing LPA versus the endogenous PI include the presence of the PI headgroup and side chain orientation of tyrosine 511 (Y511), a residue that is known to reorient upon vanilloid ligand binding to this pocket. These differences enabled us to reliably ascertain the identity of the bound ligand in the reconstruction of symmetry-expanded monomeric TRPV1 subunits..

By regrouping particles that have the same LPA binding states, we determined multiple 3D reconstructions of TRPV1 for which each has a unique LPA binding stoichiometry, including two homotetrameric conformations in which all four VBPs are occupied either by a PI or LPA, and several other

conformations in which the four VPBs are differentially occupied by LPA. For homotetrameric conformations, the final reconstructions were C4 symmetrized. For those with two LPA molecules bound in opposite subunits we applied C2 symmetry. Final maps of other conformations were reconstructed without symmetry. The accuracy of this data analysis procedure was tested previously[20]. All maps are resolved to 3.3-3.7 Å resolution.

Structures of LPA-bound substates

We refined multiple atomic models of TRPV1 against their corresponding cryo-EM density maps, in which each VBP of the tetramer is bound with either LPA or PI lipid. Among these structures, the one without LPA resembled that of TRPV1 in its resting state, as previously described[14] (Figure 1a). Similarly, the structure of TRPV1 in which all four VBPs are occupied by LPA resembles that of TRPV1 fully occupied by the potent vanilloid agonist, resiniferatoxin (RTX)[16] (Figure 1a). In this latter conformation (with LPA bound), the selectivity filter remains unchanged from the resting state, but we do see a key conformational change associated with agonist binding, namely transition of a π-helical turn in S6 to an α helical configuration (π-α transition), resulting in rotation of the lower half of the S6 helix by one residue (Figure 1b and c). Importantly, π-α transitions are seen only when agonists, but not antagonists, occupy the VBP[14,16,17]. This π-α transition rotates the gating residue L679 away from the central axis with a narrowest restriction now formed by M682 rotating into the pore. The new restriction formed by M682 mimics that formed by M641 seen above the selectivity filter of TRPV1 (Figure 1c, Supplementary Figure 2). Consistent with a previous study[16], we see a Na^+ ion coordinated to G642 in the selectivity filter, located just below M641, indicating that this configuration is ion conducting. Indeed, the B-factor surrounding M682 suggests that this residue is dynamic and thus sufficiently malleable to pass ions.

Previous functional and structural studies have identified Y511 as a key residue required for vanilloid-evoked channel activation, and its reorientation correlates with ligand binding[14,16,17]. In the case

of LPA, we also see that Y511 flips toward the VBP so that its hydroxyl group forms an H-bond with the ester carbonyl of the LPA headgroup (Figure 1d). Moreover, S512, T550, and Y554 engage in H-bond interactions with the phosphate moiety of LPA, while the free hydroxyl of the headgroup interacts with N551. In contrast, the endogenous PI lipid headgroup occupies a unique pocket below Y511, where most of its specific H-bond interactions occur (Figure 1e). Consequently, the PI lipid tails branch near Y511. Above this branchpoint the first acyl tail overlaps with the binding site of LPA and the second acyl tail sterically hinders positioning of Y511 so that it is oriented away from the VBP.

Further comparison between bound LPA and RTX shows that both form H-bonds with Y511 and T550 (Figure 1f). An important difference is that the 4-OH of the RTX vanilloid moiety engages in a bridging H-bond network between R557 and E570, two residues that form a salt bridge when TRPV1 is fully opened[14]. This reflects the fact that RTX 4-OH sits lower into the pocket, closer to R557 and E570, compared to the LPA headgroup. Therefore, the RTX headgroup may be better suited for priming this salt bridge interaction as compared to LPA, which may help to explain the greater efficacy of RTX as an agonist. Together, these structures demonstrate that LPA utilizes similar molecular interactions as other vanilloid agonists, such as RTX or capsaicin, for binding to TRPV1 and initiating gating.

Cooperativity of LPA binding

In addition to the two structures described above, we also captured structures of TRPV1 with sub-stoichiometric LPA binding, including TRPV1 bound with 1 LPA, 2 LPAs bound to either neighboring or opposite subunits, or 3 LPAs (Figure 2). It is indeed difficult to estimate the error of particle numbers in each conformation produced during a classification analysis. However, in our analysis all conformations were identified through a single round of classification of all particles in the dataset, making the error consistent among all conformations. Thus, the relative distribution of particle numbers in each of these conformations can be used to infer information about cooperativity of LPA binding. From this analysis, we infer that the first LPA binds to TRPV1 randomly, but such binding increases the affinity for binding to the adjacent versus the opposite monomer. This behavior is supported by the observation that the particle

numbers of two LPA molecules bound to opposite versus neighboring subunits is about 1:4, consistent with increased propensity for binding to an adjacent monomer.

LPA substates reveal allosteric gating

Visualizing sub-stoichiometric binding states for LPA also provides insight into intermediate steps leading to channel gating. With resting and fully liganded structures representing closed and open configurations of the pore (S6) helices, respectively (Figure 2a and b), we examined intermediate conformational states associated with sub-stochiometric LPA binding. For the convenience of description, we labeled the four subunits as A through D in a counterclockwise orientation as viewed from the extracellular face.

Binding of one LPA to subunit A does not induce an appreciable conformational change to TRPV1 other than replacement of the resident PI lipid and flipping of Y511, with no change to the pore configuration (Figure 2c). The same is true when a second LPA binds to the opposite subunit (A and C) (Figure 2d). However, when the second LPA binds to an adjacent subunit (A and B), we see gating transitions occur in the S6 helices owing to ejection of the resident PI lipid from both neighboring pockets, which communicate by virtue of domain-swap architecture (Figure 2e). Specifically, we see that one S6 helix (S6-A) is in the open configuration and the neighboring helix (S6-B) is in an intermediate position between open and closed because the resident PI lipid in the C subunit prevents full backward movement of S6-B (Figure 3a). S6-C and S6-D remain in the closed configuration (Figure 2e). The binding of the third LPA induces all four S6 helices to adopt the π-α transition, with the S6-B and S6-C in the open configuration and the S6-D and S6-A helices in intermediate positions (Figure 2f, Supplementary Figure 3). Together, these observations are consistent with a model in which ligand binding induces allosteric gating movements in the adjacent VBP through domain-swap interactions.

How does binding of LPA promote movement of S6? Reorientation of Y511 toward the VBP is a key step, allowing L674 on the S4-S5 linker to partially occupy the now vacant space, thereby facilitating

movement of the S4-S5 linker towards the VBP. Movement of the S4-S5 linker enables the S5 and S6 helices to move away from the pore axis while providing space to accommodate a π-α helix transition in S6, which is associated with the loss of hydrophobic interactions between M682 and the S4-S5 linker (Figure 3b). At the same time, reorientation of Y511 is necessary, but not sufficient to facilitate gating movements, consistent with the observation that TRPV1 antagonists also induce similar reorientation of Y511[14,17].

While the fully ligand structures obtained with LPA or RTX are similar, the intermediate configurations associated with sub-stoichiometric ligand binding are noticeably different. For example, movements of the S4-S5 linker are smaller when RTX is the agonist, and the S6 helix does not move until all four subunits are occupied[16]. One caveat to comparing LPA and RTX substates is that those observed with RTX were obtained under low-sodium conditions. Indeed, LPA-bound sub-states may be more physiologically relevant because they were obtained under normal ionic conditions, and LPA is an endogenous physiologically relevant ligand.

K710 may facilitate access of LPA to the VBP

Based on our structures and previous mutagenesis data[11], we propose that K710 is part of a basic tunnel through which LPA accesses the VBP. Indeed, when the TRPV1 structure is subjected to CAVER analysis, a tunnel is seen at the surface of the inner membrane that connects K710 to the VBP (Figure 4) and which is composed of several basic residues. The notion that this tunnel represents a conduit for LPA is consistent with the observation that channel activation is most robust when LPA is applied to excised inside-out membrane patches, providing direct access to the intracellular face of the membrane[11]. Thus, K710 may serve as a guiding residue directing LPA into this access tunnel by interacting with the negative charge of the phosphate headgroup on LPA. Capsaicin may also use this tunnel but is unaffected by the charge reversal mutation (K710D) because capsaicin is polar but neutral[11].

Using cryo-EM to capture snapshots of LPA binding to TRPV1, we have been able to determine how this endogenous inflammatory agonist binds to the VBP to induce conformational transitions associated with channel gating. While early mutagenesis studies suggested that K710 marks the site of LPA binding, our structures now show that this residue may, instead, affect access of LPA to its true binding site within the VBP. By capturing sub-saturating states of LPA binding, we uncovered structural underpinnings of allosteric gating associated with LPA binding that may be relevant to the action of other endogenous agonists.

Author contributions. WRA conceived the project, performed cryo-EM experiments, and analyzed data. YC and DJ provided guidance throughout. All authors contributed to manuscript preparation.

Acknowledgements. We thank Dr. David Bulkley and Glenn Gilbert of the UCSF EM Core Facility for help with cryo-EM data acquisition, Ms. Yifei Chen for help with part of data processing. Funding was provided by an IRACDA NIH Training Award (K12GM081266 to W.R.A.) and NIH grants (R35NS105038 to D.J. and 1R35GM140847 to Y.C.). Y.C. is an investigator of Howard Hughes Medical Institute.

Conflicts of interest. There are no conflicts of interest regarding the work presented in this manuscript.

METHODS

Materials. Reagents were purchased from Sigma-Aldrich (St. Louis, MO, USA) unless noted below. 18:1 Lysophosphatidic acid [(2-hydroxy-3-phosphonooxypropyl) (*Z*)-octadeca-9-enoate] was purchased from Cayman Chemical Company (Ann Arbor, MI, USA) for cryo-EM sample prep and diluted in DMSO or dried and dissolved in chloroform:methanol:water 20:9:1 (v:v:v) ("PIP Mixture", Avanti Polar Lipids,

Birmingham, AL, USA) for electrophysiology. Soy polar lipid extract was purchased from Avanti Polar Lipids. Bio-beads SM2 was purchased from Bio-Rad (Hercules, CA, USA). Freestyle 293 Expression Medium was purchased from Gibco. Sf9 and insect cell culture media were purchased from Expression Systems (Davis, CA, USA). Fetal bovine serum was purchased from PEAK (Wellington, CO, USA) and bovine calf serum was purchased from HyClone (Marlborough, MA, USA). HEK293 GnTI$^-$ cells and HEK293T cells were purchased from ATCC (Manassas, VA, USA). DH5α competent cells were purchased from New England Biolabs (Ipswich, MA, USA). Quantifoil® R1.2/1.3 Au 300 mesh grids were purchased from Quantifoil Micro Tools GmbH (Großlöbichau, Germany).

Protein purification and nanodisc reconstitution. Recombinant minimal functional rat TRPV1 (residues 110-603 and 627-764) was expressed in HEK293 GnTI$^-$ cells and purified as previously described[15]. The membrane scaffold protein, MSP2N2, for nanodisc reconstitution was expressed in *E. coli* as previously described[14]. For nanodisc reconstitution, soybean polar lipids were dried down under a gentle stream of N_2 gas in borosilicate glass tubes and resuspended in 20 mM N-dodecyl-β-D-maltoside (DDM). Purified TRPV1 in DDM was added with MSP2N2 and lipids to a final mole ratio of 1:20:674. The detergent was removed using 2 batches of Bio-Beads SM2 with rotation overnight at 4° C overnight. The MPB and His tags on TRPV1 and MSP2N2, respectively, was removed with TEV protease for 4 hrs before size-exclusion chromatography purification of the TRPV1-nanodiscs using a Superdex 200 Increase 10/300 GL column (GE) on an Akta FPLC. Mobile phase consisted of 20 mM HEPES · NaOH (pH 7.5), 150 mM NaCl, and 0.1 mM tris(2-carboxyethyl)phosphine hydrochloride (TCEP · HCl). Peak fractions were pooled and concentrated to 2.1 $mg \cdot mL^{-1}$ using an Amicon Ultra filter device (100-kDa MWCO, Millipore) and analyzed by SDS-PAGE and negative-stain EM. Prior to sample preparation for cryo-EM, LPA (DMSO) was added to 12 μL TRPV1-nanodisc sample to a final concentration of 25 μM (0.5% vehicle final) for 30 min at room temperature.

EM sample preparation and data acquisition.

For negative-stain EM, TRPV1-nanodisc sample (3 μL at 40 μg · mL^{-1}) was applied on glow-discharged Cu grids covered by continuous carbon film and stained with 0.75% (w/v) uranyl formate (Ohi, et al. 2004). Sample was imaged on a Tecnai T12 microscope (ThermoFisher FEI company) operated at 120 kV at 52,000 × magnification using an UltraScan 4000 camera (Gatan), which corresponds to a 2.21 Å pixel size.

For cryo-EM, 3 μL of LPA-incubated TRPV1-nanodiscs was applied to glow-discharged Quantifoil R1.2/1.3 Au 300 mesh grids covered in holey carbon film and blotted with Whatman 1 filter paper on a Vitrobot Mark IV (FEI company) with a 4.5 s blotting time, 4 blot force, and 100% humidity at 25° C, and subsequentially plunge-frozen in liquid ethane cooled by liquid nitrogen. Sample was imaged with a Titan Krios microscope (ThermoFisher FEI) operated at 300 kV and equipped with a Bio Quantum post-column energy filter with zero-loss energy selection slit set to 20 eV and a K3 camera (Gatan). Data collection was carried out with SerialEM software (Mastronarde, 2005). Data acquisition parameters are given in Supplementary Table 1.

Image processing.

A visual scheme of the image processing is given as Supplementary Figure 1. Motion correction on movie stacks was processed on-the-fly using MotionCorr2[21] and binned 2 × 2 with Fourier cropping. Dose-weighted micrographs were manually culled for imperfections (broken grids, opaque ice, carbon content, and failed motion correction) before importing into cryoSPARC[22] for data processing. Micrographs were CTF-corrected using Patch-based CTF Estimation and subsequentially whitelisted for further processing using a cutoff resolution of < 4.5 Å. EMD-8118 (resting TRPV1 in nanodisc) was used to make 25 templates for template picking. Picks were extracted and binned 4 × 4 using Fourier cropping and reference-free 2D classification was used to remove non-TRPV1-nanodisc picks. Extracted particles were then imported into RELION[23] and subjected to 2 rounds of reference-based 3D classification (ref. EMD-8118, low-pass filtered 12 Å) to remove low-resolution and featureless particles. Selected classes were combined and refined using 3D Auto Refine with C4 symmetry in RELION using EMD-8118 as a reference

(low-pass filter 12 Å). Ligand heterogeneity could not be separated at this stage and so particles were further processed using focused classification on the vanilloid binding pocket.

Focused classification was carried out as previously described[20]. The 3D-refined particles were symmetry-expanded using C4 symmetry and a mask focused on the vanilloid binding pocket was used for particle subtraction and 3D classification on the symmetry-expanded particles. Classification parameters: ref. EMD-8118 (no low-pass filter), Regularization Parameter T = 80, symmetry C1, no image alignment. Classes were whitelisted for further processing based on clarity of the ligand features and the ligand content (LPA or lipid) was visually assigned to each class. Particles were organized based on ligand content and then star files were generated for the original tetramers based on the content of LPA-bound vanilloid pockets (LPAx0, LPAx1, LPAx2, LPAx3, and LPAx4). LPAx0 and LPAx4 were imported into cryoSPARC for non-uniform refinement and then sharpened using PHENIX[24] half-map sharpening.

For LPAx1, LPAx2, and LPAx3, a script was generated to select the copy of the symmetry-expanded particles in which the particles are aligned with the LPA pockets onto each other. We further separated LPAx2 into particles in which the LPA monomers are bound next to each other (LPAx2 vicinal) and particles in which the LPA monomers are bound across from each other (LPAx2 distal). These pre-aligned particles were then imported into RELION for further processing. LPAx1, LPAx2 vicinal, and LPAx3 were refined using local refinements and using a mask focused on the transmembrane region (ref. EMD-8118, low-pass filtered 5 Å). Resulting maps were sharpened using RELION Post-Process and the transmembrane mask was used as the solvent mask. For LPX2 distal, particles were first subjected to 3D classification using 1 class, Regularization Parameter T = 40, symmetry C2, transmembrane mask, and local searches to obtain the initial angles. The star file and resulting map were used in 3D Auto Refine as the input star file and the reference (low-pass filtered to the classification resolution of 4.1 Å), respectively, and refinement was carried out using a transmembrane mask and local searches. The resulting map was sharpened using RELION Post-Process and the transmembrane mask as the solvent mask.

Model building. Resting TRPV1 (PDB-7L2P) was used as the starting model and amino acids were added or removed based on the resolvable features of the data herein. The starting model was initially docked into the resulting sharpened maps using UCSF Chimera[25]. PDB and molecular restraint files for LPA and the resident lipid were generated in PHENIX using eLBOW, and then LPA or the resident were manually docked into the ligand densities. For the resident lipid, di-palmitoyl phosphatidylinositol was used as the starting structure and then the tails were shortened to fit the resolvable density. Models were refined using several iterations of PHENIX Real Space Refine and manual adjustments in COOT[26]. The quality of the refined models was determined using the Comprehensive Model Function in PHENIX and the results are shown in Table 1.

Pore radius determination, tunnel analysis, electrostatics calculation, and structural figures. The pore radius for LPAx0 and LPAx4 was determined using the HOLE program[27] and plotted in Excel. Tunnels within TRPV1 were identified, visualized, and made into a figure using the program CAVER[28]. Surface electrostatic charge determination was performed, visualized, and made into a figure in PyMOL. All other structural figures were made using UCSF ChimeraX[29,30] and PowerPoint.

REFERENCES

1 Caterina, M. J. *et al.* The capsaicin receptor: a heat-activated ion channel in the pain pathway. *Nature* **389**, 816-824 (1997). https://doi.org:10.1038/39807

2 Jordt, S. E., Tominaga, M. & Julius, D. Acid potentiation of the capsaicin receptor determined by a key extracellular site. *Proc Natl Acad Sci U S A* **97**, 8134-8139 (2000). https://doi.org:10.1073/pnas.100129497

3 Rohacs, T. Phosphoinositide regulation of TRPV1 revisited. *Pflugers Arch* **467**, 1851-1869 (2015). https://doi.org:10.1007/s00424-015-1695-3

4 Starowicz, K., Nigam, S. & Di Marzo, V. Biochemistry and pharmacology of endovanilloids. *Pharmacol Ther* **114**, 13-33 (2007). https://doi.org:10.1016/j.pharmthera.2007.01.005

5 Tominaga, M. *et al.* The cloned capsaicin receptor integrates multiple pain-producing stimuli. *Neuron* **21**, 531-543 (1998). https://doi.org:10.1016/s0896-6273(00)80564-4

6 Morales-Lazaro, S. L. & Rosenbaum, T. A painful link between the TRPV1 channel and lysophosphatidic acid. *Life Sci* **125**, 15-24 (2015). https://doi.org:10.1016/j.lfs.2014.10.004

7 Ciardo, M. G. & Ferrer-Montiel, A. Lipids as central modulators of sensory TRP channels. *Bba-Biomembranes* **1859**, 1615-1628 (2017). https://doi.org:10.1016/j.bbamem.2017.04.012

8 Bujak, J. K., Kosmala, D., Szopa, I. M., Majchrzak, K. & Bednarczyk, P. Inflammation, Cancer and Immunity-Implication of TRPV1 Channel. *Front Oncol* **9**, 1087 (2019). https://doi.org:10.3389/fonc.2019.01087

9 Geraldo, L. H. M. *et al.* Role of lysophosphatidic acid and its receptors in health and disease: novel therapeutic strategies. *Signal Transduct Target Ther* **6**, 45 (2021). https://doi.org:10.1038/s41392-020-00367-5
10 Pan, H. L., Zhang, Y. Q. & Zhao, Z. Q. Involvement of lysophosphatidic acid in bone cancer pain by potentiation of TRPV1 via PKCepsilon pathway in dorsal root ganglion neurons. *Mol Pain* **6**, 85 (2010). https://doi.org:10.1186/1744-8069-6-85
11 Nieto-Posadas, A. *et al.* Lysophosphatidic acid directly activates TRPV1 through a C-terminal binding site (vol 8, pg 78, 2012). *Nat Chem Biol* **8**, 737-737 (2012). https://doi.org:10.1038/nchembio0812-737c
12 Cao, E., Cordero-Morales, J. F., Liu, B., Qin, F. & Julius, D. TRPV1 channels are intrinsically heat sensitive and negatively regulated by phosphoinositide lipids. *Neuron* **77**, 667-679 (2013). https://doi.org:10.1016/j.neuron.2012.12.016
13 Cao, E. H., Liao, M. F., Cheng, Y. F. & Julius, D. TRPV1 structures in distinct conformations reveal activation mechanisms. *Nature* **504**, 113-+ (2013). https://doi.org:10.1038/nature12823
14 Gao, Y., Cao, E., Julius, D. & Cheng, Y. TRPV1 structures in nanodiscs reveal mechanisms of ligand and lipid action. *Nature* **534**, 347-351 (2016). https://doi.org:10.1038/nature17964
15 Liao, M., Cao, E., Julius, D. & Cheng, Y. Structure of the TRPV1 ion channel determined by electron cryo-microscopy. *Nature* **504**, 107-112 (2013). https://doi.org:10.1038/nature12822
16 Zhang, K., Julius, D. & Cheng, Y. Structural snapshots of TRPV1 reveal mechanism of polymodal functionality. *Cell* (2021). https://doi.org:10.1016/j.cell.2021.08.012
17 Neuberger, A. *et al.* Human TRPV1 structure and inhibition by the analgesic SB-366791. *Nat Commun* **14**, 2451 (2023). https://doi.org:10.1038/s41467-023-38162-9
18 Kwon, D. H., Zhang, F., Fedor, J. G., Suo, Y. & Lee, S. Y. Vanilloid-dependent TRPV1 opening trajectory from cryoEM ensemble analysis. *Nat Commun* **13**, 2874 (2022). https://doi.org:10.1038/s41467-022-30602-2
19 Jordt, S. E. & Julius, D. Molecular basis for species-specific sensitivity to "hot" chili peppers. *Cell* **108**, 421-430 (2002). https://doi.org:Doi 10.1016/S0092-8674(02)00637-2
20 Arnold, W. R., Asarnow, D. & Cheng, Y. Classifying liganded states in heterogeneous single-particle cryo-EM datasets. *Microscopy (Oxf)* **71**, i23-i29 (2022). https://doi.org:10.1093/jmicro/dfab044
21 Zheng, S. Q. *et al.* MotionCor2: anisotropic correction of beam-induced motion for improved cryo-electron microscopy. *Nat Methods* **14**, 331-332 (2017). https://doi.org:10.1038/nmeth.4193
22 Punjani, A., Rubinstein, J. L., Fleet, D. J. & Brubaker, M. A. cryoSPARC: algorithms for rapid unsupervised cryo-EM structure determination. *Nat Methods* **14**, 290-296 (2017). https://doi.org:10.1038/nmeth.4169
23 Scheres, S. H. RELION: implementation of a Bayesian approach to cryo-EM structure determination. *J Struct Biol* **180**, 519-530 (2012). https://doi.org:10.1016/j.jsb.2012.09.006
24 Liebschner, D. *et al.* Macromolecular structure determination using X-rays, neutrons and electrons: recent developments in Phenix. *Acta Crystallogr D* **75**, 861-877 (2019). https://doi.org:10.1107/S2059798319011471
25 Pettersen, E. F. *et al.* UCSF Chimera--a visualization system for exploratory research and analysis. *J Comput Chem* **25**, 1605-1612 (2004). https://doi.org:10.1002/jcc.20084
26 Emsley, P., Lohkamp, B., Scott, W. G. & Cowtan, K. Features and development of Coot. *Acta Crystallographica Section D-Biological Crystallography* **66**, 486-501 (2010). https://doi.org:10.1107/S0907444910007493
27 Smart, O. S., Neduvelil, J. G., Wang, X., Wallace, B. A. & Sansom, M. S. HOLE: a program for the analysis of the pore dimensions of ion channel structural models. *J Mol Graph* **14**, 354-360, 376 (1996). https://doi.org:10.1016/s0263-7855(97)00009-x
28 Jurcik, A. *et al.* CAVER Analyst 2.0: analysis and visualization of channels and tunnels in protein structures and molecular dynamics trajectories. *Bioinformatics* **34**, 3586-3588 (2018). https://doi.org:10.1093/bioinformatics/bty386

29 Goddard, T. D. *et al.* UCSF ChimeraX: Meeting modern challenges in visualization and analysis. *Protein Sci* **27**, 14-25 (2018). https://doi.org:10.1002/pro.3235

30 Pettersen, E. F. *et al.* UCSF ChimeraX: Structure visualization for researchers, educators, and developers. *Protein Sci* **30**, 70-82 (2021). https://doi.org:10.1002/pro.3943

FIGURES

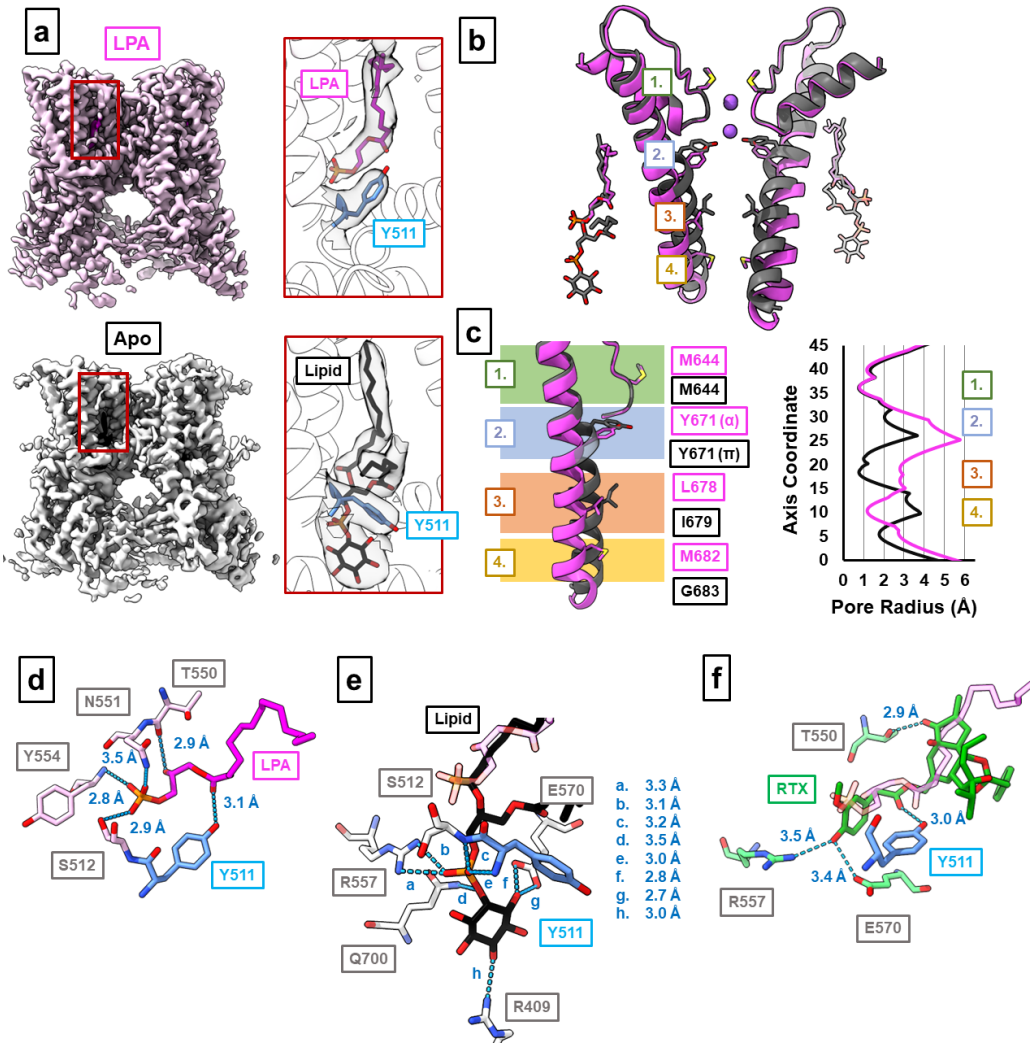

Figure 1. *Structures of apo and LPA bound TRPV1.* **(a)** Maps of TRPV1 bound with 4 LPA molecules (resolution 3.5 Å) or 4 endogenous PI lipid molecules (Apo) in the VBP (resolution 3.3 Å). Insets show densities of ligand and Y511. **(b)** Pore dilation and opening elicited by LPA binding. Features highlighted include: 1) M644; 2) Y671 helical transition; 3) I679 to L678 transition; 4) G683 to M682 transition. **(c)** Pore radius as determined by the HOLE program. Numbers correspond to the same features highlighted in panel 1d. **(d-f)** Electrostatic interactions between residues in the VBP and LPA (d), PI lipid (e), or RTX (f, PDB-7MZD).

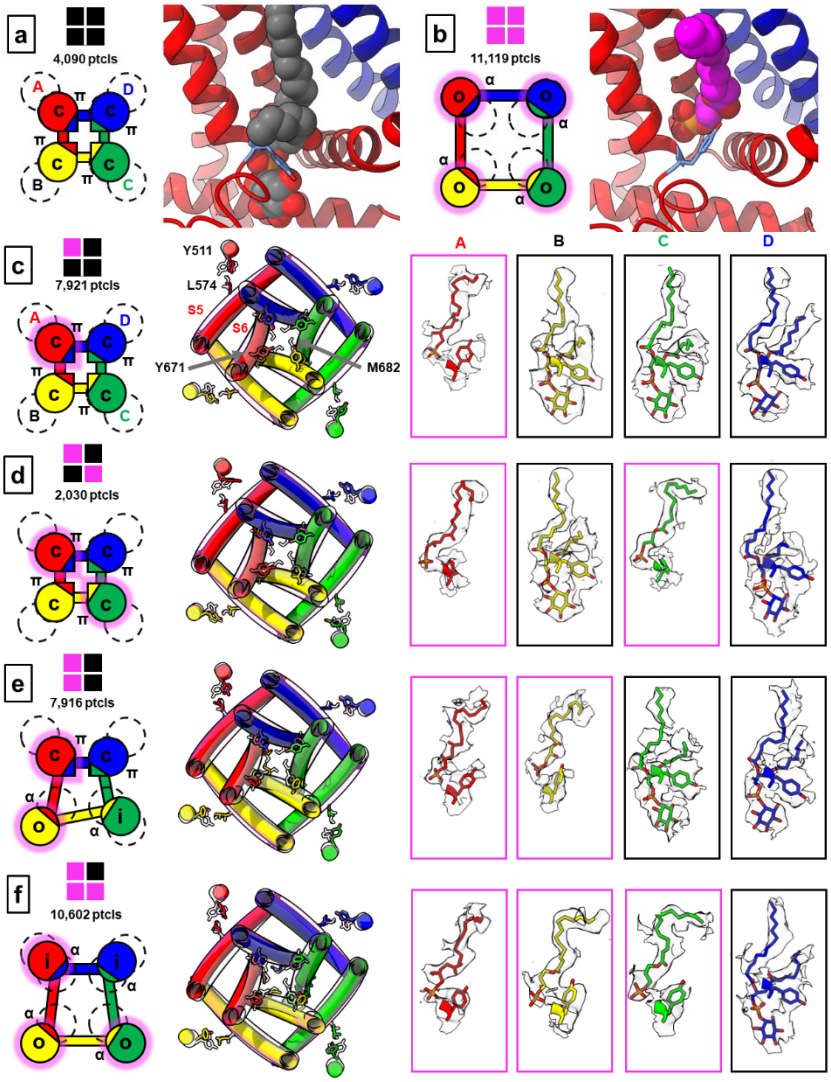

Figure 2. *Sub-stoichiometric states of LPA binding.* **(a)**the closed configuration of TRPV1 with all four subunits occupied by PI lipid. **(b)** open configuration TRPV1 with LPA bound to all four subunits. The VBPs of the A monomers are shown to demonstrate the domain-swap architecture that comprises the VBP (S3, S4, and S4-S5 from A; S5 and S6 from D). **(c-f)** Models of the sub-saturating binding states. Leftmost panels show a cartoon representation of the TRPV1 tetramer highlighting the functional state of each VBP monomer (o, open; c, closed; i, intermediate), the domain swap of the pore helices, and the helical state of Y671 (π or α). Chains are colored and labeled according to the liganded state of the monomer. Monomers are labeled anticlockwise, LPA occupied monomers are shadowed with magenta. Tube models of the S5 and S6 helices along with Y511 are also shown. Ghosts of the LPAx0 (black) and LPAx4 (magenta) are

provided for comparison. Rightmost panels show the corresponding VBPs along with the densities for the ligand and Y511. VBPs containing LPA are outlined with magenta.

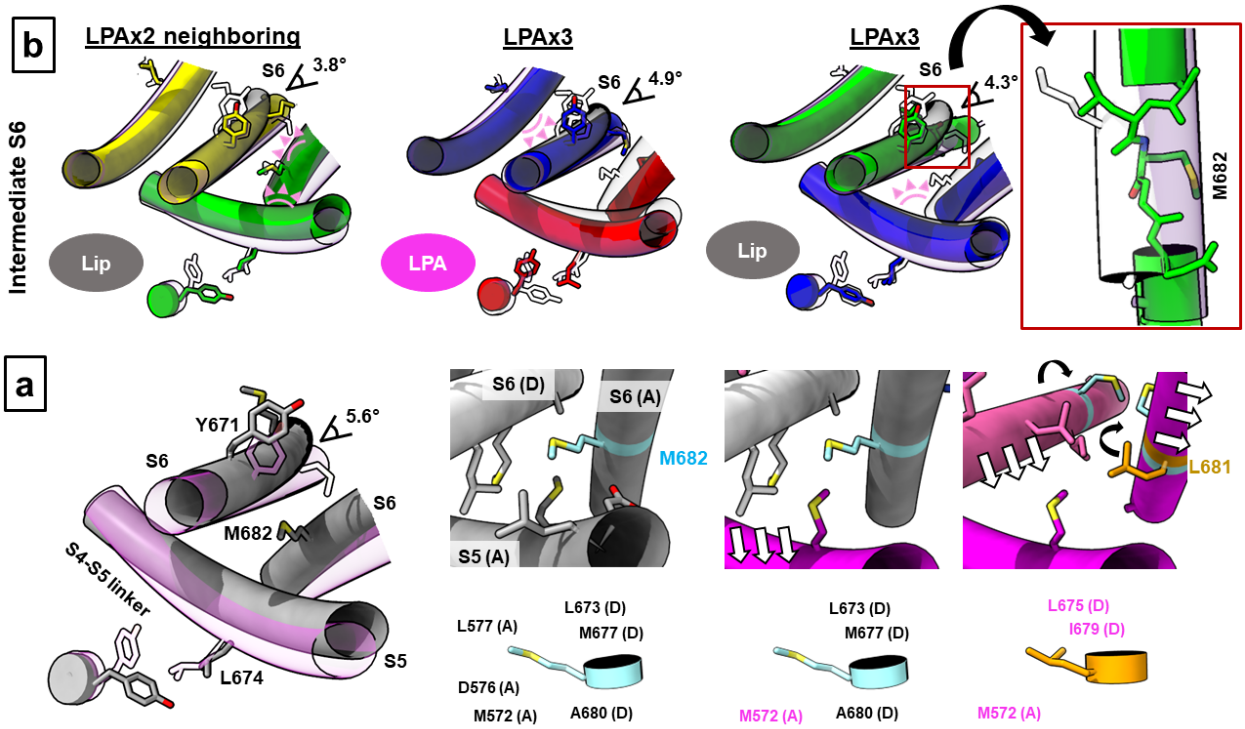

Figure 3. *Intermediate states and mechanism of allostery* **(a)** Intermediate states of the S6 helices. Steric clashes preventing full opening of the S6 helix are shown as pink triangles. Angles of opening are shown as a measure of the intermediate state. For LPAx3, the S6-C helix is distorted from a typical α-helical structure. **(b)** Proposed mechanism for the LPA-induced opening of TRPV1 as the channel goes from apo state (grey) to one completely occupied by LPA (magenta). Residues in contact with M682 (< 5.0 Å) as it switches positions with L681 due to the π-α helix transition are highlighted. The S6 helix tilts by 5.6° during the transition from closed to open states.

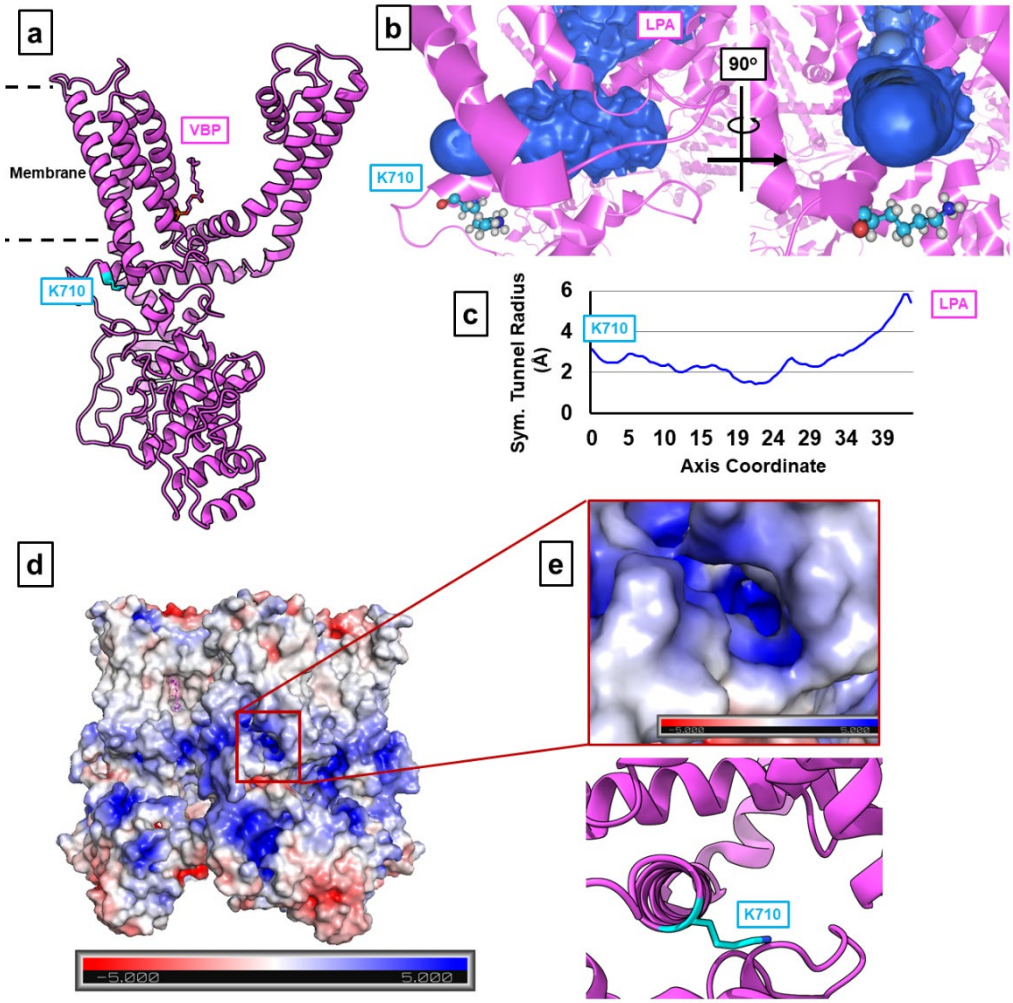

Figure 4. *K710 marks a potential ingress tunnel for LPA*. **(a)** K710 (blue) sits near the membrane surface and approximately 20 Å away from the VBP. **(b)** An access tunnel (blue) connecting K710 to the VBP as identified by the program CAVER. **(c)** Size of the tunnel as determined from CAVER. **(d)** Surface charge map of TRPV1 with location of putative tunnel indicated by red box. **(e)** Surface charge map of the tunnel identified by CAVER with the corresponding model of TRPV1-LPAx4 below.